



Research Publication Repository

<http://publications.wehi.edu.au/search/SearchPublications>

This is the author's peer reviewed manuscript version of a work accepted for publication.

Publication details:	Gruszczyk J, Huang RK, Chan LJ, Menant S, Hong C, Murphy JM, Mok YF, Griffin MDW, Pearson RD, Wong W, Cowman AF, Yu Z, Tham WH. Cryo-EM structure of an essential <i>Plasmodium vivax</i> invasion complex. <i>Nature</i> . 2018 559(7712):135-139
Published version is available at:	https://doi.org/10.1038/s41586-018-0249-1

Changes introduced as a result of publishing processes such as copy-editing and formatting may not be reflected in this manuscript.

1 **Cryo-EM structure of an essential *Plasmodium vivax* invasion complex**

2

3 Jakub Gruszczyk^{1†}, Rick K. Huang^{2†}, Li-Jin Chan^{1,3}, Sébastien Menant¹, Chuan
4 Hong², James M. Murphy^{1,3}, Yee-Foong Mok⁴, Michael D.W. Griffin⁴, Richard D.
5 Pearson^{5,6}, Wilson Wong¹, Alan F. Cowman^{1,3}, Zhiheng Yu^{2*}, Wai-Hong Tham^{1,3,*}

6 ¹The Walter and Eliza Hall Institute of Medical Research, Parkville, Victoria 3052,
7 Australia.

8

9 ²CryoEM Shared Resources, Janelia Farm Research Campus, Howard Hughes
10 Medical Institute, Ashburn, Virginia 20147, USA.

11

12 ³Department of Medical Biology, The University of Melbourne, Melbourne, Victoria
13 3010, Australia.

14

15 ⁴Department of Biochemistry and Molecular Biology, Bio21 Molecular Science and
16 Biotechnology Institute, The University of Melbourne, Melbourne, Victoria 3010,
17 Australia.

18

19 ⁵Wellcome Trust Sanger Institute, Hinxton, Cambridge, United Kingdom.

20

21 ⁶Big Data Institute, Li Ka Shing Centre for Health Information and Discovery,
22 Oxford, United Kingdom.

23

24 † These authors contributed equally to this work

25

26 *Co-corresponding authors:

27 **Wai-Hong Tham**

28 Division of Infection and Immunity
29 The Walter and Eliza Hall Institute
30 Tel: +61430044842
31 Email: tham@wehi.edu.au

32 **Zhiheng Yu**

33 CryoEM Shared Resource
34 Janelia Farm Research Campus,
35 Howard Hughes Medical Institute
36 Email: yuz@janelia.hhmi.org

37

38

39

40

41

42 **Summary**

43 *Plasmodium vivax* is the most widely distributed malaria parasite that
44 infects humans¹. It exclusively invades reticulocytes and successful entry depends
45 on the specific interactions between *P. vivax* reticulocyte-binding protein 2b
46 (PvRBP2b) and transferrin receptor 1 (TfR1)². The PvRBP2b-TfR1 invasion
47 pathway is essential for *P. vivax* entry into human reticulocytes, as TfR1-
48 deficient erythroid cells are refractory to invasion by *P. vivax*, and anti-PvRBP2b
49 monoclonal antibodies inhibit reticulocyte-binding and block *P. vivax* invasion in
50 field isolates². Here we report a high-resolution structure of a ternary complex
51 with PvRBP2b bound to human TfR1 and transferrin, at 3.7 Å resolution by
52 cryo-electron microscopy. Mutational analyses show that PvRBP2b residues
53 involved in complex formation are conserved, providing a promising design
54 strategy to engineer antigens that may be strain-transcendent against *P. vivax*
55 infection. Functional analyses of TfR1 highlight how *P. vivax* has hijacked TfR1,
56 which is an essential housekeeping protein, by binding to sites that govern host
57 specificity without affecting its cellular function of transporting iron. Crystal and
58 solution structures of PvRBP2b in complex with antibody fragments
59 characterize the inhibitory epitopes. Our results establish a structural
60 framework for understanding how *P. vivax* reticulocyte-binding protein engages
61 its receptor and the molecular mechanism of inhibitory monoclonal antibodies,
62 providing important information for the design of novel vaccine candidates.

63

64

65

66

67 **Main text**

68 Red blood cell invasion is an essential step in the malaria parasite's lifecycle
69 and depends on interactions between parasite invasion ligands and their cognate red
70 blood cell receptors²⁻⁹. *Plasmodium vivax* invades reticulocytes^{10,11} and a family of
71 parasite adhesins called the *P. vivax* reticulocyte-binding protein (PvRBP) play a
72 crucial role in reticulocyte recognition¹²⁻¹⁴. One major invasion pathway for *P. vivax*
73 entry into reticulocytes is mediated by the specific interaction between a member of
74 this protein family, PvRBP2b, and the essential housekeeping protein transferrin
75 receptor 1 (TfR1)².

76 We expressed and purified a recombinant fragment of PvRBP2b
77 encompassing residues 161-969 (PvRBP2b₁₆₁₋₉₆₉) in complex with TfR1 and Tf, and
78 reconstructed a three-dimensional electron density map using cryo-electron
79 microscopy (cryo-EM) (Extended Data Fig. 1 and Extended Data Table 1). The
80 electron density corresponding to residues 161-167 and 634-969 could not be
81 observed. The remaining residues 168 to 633 (PvRBP2b₁₆₈₋₆₃₃) adopt a highly
82 elongated, predominantly α -helical fold that can be subdivided into two domains
83 denoted as N- and C-terminal domains with an angle of $\sim 130^\circ$ between them (Fig.
84 1a). The N-terminal domain encompassing residues 168-460 and helices $\alpha 1$ to $\alpha 7$,
85 can be superimposed with the crystal structure of the corresponding fragment (PDB
86 accession number 5W53)² with root mean square deviation (RMSD) of 0.84 Å over
87 279 aligned C α atoms (Extended Data Fig. 2a). The structure of the C-terminal
88 domain encompassing residues 461-633 was determined *de novo* and consists of a
89 bundle of three long helices denoted as $\alpha 8$, $\alpha 9$ and $\alpha 10$ (Fig. 1a). The N-terminal
90 domain is predominantly positively charged, in contrast to the negatively charged C-
91 terminal domain (Extended Data Fig. 2b).

92 The cryo-EM structure of the PvRBP2b-TfR1-Tf ternary complex was
93 determined to an overall resolution of 3.7 Å (Fig. 1b and Extended Data Fig. 1). The
94 size of the resolved structure is approximately 150 Å in its longest dimension, and
95 120 and 140 Å in the other two dimensions (Fig. 1b). The PvRBP2b-TfR1-Tf
96 complex consists of the homodimeric TfR1 (residues 120-760) and its corresponding
97 two molecules of iron bound-Tf (residues 1-679), with two molecules of PvRBP2b
98 bound on either side (Fig. 1c). We performed analytical ultracentrifugation
99 experiments using a fixed amount of TfR1-Tf in the presence of increasing
100 concentrations of PvRBP2b (Extended Data Fig. 2c-e). These data are consistent with
101 the binding of two molecules of PvRBP2b to the TfR1-Tf complex with macroscopic
102 dissociation constants in the mid-nanomolar to low-micromolar range. We determined
103 another structure with only one PvRBP2b protein bound to the TfR1-Tf binary
104 complex allowing us to observe the conformational changes induced in the receptor
105 upon ligand binding (Extended Data Fig. 3a-e). Additional classification further
106 separated the two-ligand complex into two subclasses, which indicate an intrinsic
107 flexibility of the N-terminal domain (Extended Data Fig. 3f, g). Overall, binding of
108 PvRBP2b results in small conformational changes confined to the apical domain of
109 TfR1 that mostly involve rearrangement of the loops on the tip of the domain.

110 TfR1 is a single pass type II transmembrane protein, with a cytoplasmic
111 domain and a large extracellular domain¹⁵. The extracellular domain has a protease-
112 like domain which resides proximal to the membrane, a helical domain responsible
113 for dimerization, and an apical domain of unknown function (Fig. 1c). Co-crystal
114 structures have been solved of either human TfR1 in complex with Tf or HFE, or with
115 the entry glycoprotein of a New World hemorrhagic arenavirus, Machupo virus
116 (MACV GP1)¹⁶⁻¹⁹. The cryo-EM structure of the PvRBP2b-TfR1-Tf complex shows

117 that PvRBP2b interacts with the TfR1-Tf binary complex through three principal
118 sites; i) the apical domain of TfR1, ii) the protease-like domain of TfR1 and iii) the N-
119 terminal region of Tf (Fig. 2a-c and Extended Data Table 2). When bound to
120 PvRBP2b, TfR1 shows a more extensive buried surface area ($\sim 1,271 \text{ \AA}^2$) compared to
121 Tf ($\sim 386 \text{ \AA}^2$) (Fig. 2a). We mapped naturally occurring field polymorphisms using
122 data from the MalariaGEN *P. vivax* Genome Variation project onto the PvRBP2b₁₆₈₋
123 ₆₃₃ structure (Fig. 2d,e)^{2,20}. Our results show that residues in PvRBP2b that interact
124 with TfR1 and Tf are mostly conserved, but reside within a region that is under
125 balancing selection^{2,20}.

126 We performed site-directed mutagenesis to identify residues at the PvRBP2b-
127 TfR1 interface critical for complex formation (Extended Data Fig. 4a, b). We mutated
128 the following residues on PvRBP2b that interact with TfR1, R359, E530, D531,
129 Y538, Y542, E556, K563, K600, Y604, to alanine. These residues were chosen as
130 they were involved in either the formation of salt bridges or as part of the three-
131 tyrosine motif (Fig. 2c). We also mutated four PvRBP2b residues that interact with
132 Tf, Y186, K297, R304 and N428 to alanine. Of all the aforementioned mutants, only
133 PvRBP2b_{Y542A}, PvRBP2b_{K600A} and PvRBP2b_{Y604A} showed a $\sim 80\%$ reduction in
134 binding to reticulocytes compared to wildtype (Fig. 3a).

135 We examined the ability of these PvRBP2b mutant proteins to form a stable
136 complex with TfR1-Tf using analytical SEC. As a control, we used TfR1 with a
137 deletion in glycine 217 (TfR1 Δ G217) which is known abolish complex formation².
138 While TfR1 Δ G217 is able to bind Tf, ternary complex formation with PvRBP2b was
139 not detected compared to wildtype (Fig. 3b-d). For all PvRBP2b mutants, only
140 PvRBP2b_{Y542A}, PvRBP2b_{K600A} and PvRBP2b_{Y604A} were defective in forming a
141 complex with TfR1-Tf, as indicated by an overlap of elution profiles with

142 TfR1 Δ G217 (Fig. 3b, c). We examined if stacking interactions mediated by the three-
143 tyrosine motif at PvRBP2b residues Y538, Y542 and Y604, were important for
144 complex formation (Fig. 2c, top middle panel). Our results indicate the hydrogen
145 bonds formed by residue Y542 and the stacking interactions formed by aromatic side
146 chains of Y538 and Y604 play an important role in PvRBP2b interaction with TfR1
147 (Extended Data Fig. 4c). To examine the importance of the salt bridge at residue
148 PvRBP2b_{K600} (Fig. 2c, top right panel), we generated both PvRBP2b_{K600E} and
149 PvRBP2b_{K600M} mutants, which have similar side chain lengths but lack the ability to
150 form salt bridges. Both these mutants were defective in complex formation,
151 supporting the importance of the salt bridge formed by the residue K600 (Extended
152 Data Fig. 4c). These results indicate that PvRBP2b residues Y542, K600 and Y604 are
153 critical for reticulocyte-binding and complex formation.

154 We mutated the following residues on TfR1, E149, R208, Y211, E214, E294,
155 K574 and E578, to alanine. We also modified S142 to glycine to mimic a common
156 polymorphism in TfR1 that is prevalent in Asian populations, and N348 to alanine as
157 it is a critical determinant for MACV GP1 engagement with TfR1^{17,21}. The overall
158 structure of TfR1 is unperturbed by these single site mutations based on circular
159 dichroism analyses and the observation that all TfR1 mutants retain their ability to
160 bind Tf (Extended Data Fig. 4d-f). Of all the aforementioned mutants, only
161 TfR1_{Y211A}, TfR1_{E294A} and TfR1_{E149A} mutants were not able to bind to PvRBP2b, as
162 indicated by an overlap of elution profiles with TfR1 Δ G217 (Fig. 3d).

163 Our structure-function analyses pinpoint three key interactions important for
164 complex assembly; the interactions formed by PvRBP2b_{Y542} and TfR1_{Y211}, a salt
165 bridge formed between PvRBP2b_{K600} and TfR1_{E294} and a second salt bridge between
166 TfR1_{E149} and PvRBP2b_{R359} (Fig. 3e). Y211 is localized in the strand β II-2 of TfR1's

167 apical domain and is a critical residue for entry of New World hemorrhagic
168 arenaviruses²². Furthermore, TfR1_{Y211} and TfR1_{E149} are only present in human TfR1
169 but not mouse TfR1, providing an explanation of how *P. vivax* invasion is not
170 permissive into rodent reticulocytes (Extended Data Fig. 5a, b)^{21,23}. We show that
171 PvRBP2b does not bind to TfR1-Tf binary complexes containing either mouse TfR1
172 or mouse Tf, indicating that PvRBP2b displays specificity for human TfR1 and
173 human Tf (Extended Data Fig. 5c). While the majority of PvRBP2b interactions
174 involve TfR1, we propose that interactions with Tf are important for complex stability
175 as only the PvRBP2b-TfR1-Tf ternary complex was isolated by size exclusion
176 chromatography and visualized by cryo-EM techniques. These results show that
177 PvRBP2b binds to TfR1 residues not involved with Tf binding and identifies TfR1
178 residues implicated in *P. vivax* specificity for human reticulocytes.

179 Anti-PvRBP2b monoclonal antibodies, 3E9, 6H1 and 10B12, inhibit
180 PvRBP2b binding to reticulocytes and block the invasion of *P. vivax* into
181 reticulocytes². We identified an additional mAb, 4F7 that inhibits PvRBP2b binding
182 to reticulocytes (Fig. 4a, Extended Data Fig. 6a). As expected, non-inhibitory anti-
183 PvRBP2b mAb 8G7 and anti-PfRh4 mAb 10C9 did not affect PvRBP2b binding (Fig.
184 4a)². We obtained crystal structures for PvRBP2b-3E9, PvRBP2b-4F7 and PvRBP2b-
185 6H1 complexes refined to 2.53, 2.66 and 3.34 Å respectively, while a model for
186 PvRBP2b-10B12 was derived from SAXS analysis (Fig. 4b-d, Extended Data Fig.
187 6b-f, Extended Data Table 3 and Extended Data Table 4). 3E9 binds on the side of the
188 N-terminal domain of PvRBP2b to a region localized between three helices $\alpha 4$, $\alpha 5$
189 and $\alpha 6$ (Fig. 4b,c). The binding sites for 6H1 and 4F7 antibody fragments overlap and
190 they bind close to the tip of the N-terminal domain of PvRBP2b, forming interactions
191 with the residues localized in helix $\alpha 2$ and $\alpha 3$ as well as to the loop interconnecting

192 helices $\alpha 3$ and $\alpha 4$ (Fig. 4b, c). 10B12 binds at the tip of PvRBP2b at a distinct site
193 from 6H1 and 4F7 (Fig. 4b, c). When superimposed on the ternary complex structure
194 (Fig. 4c, d), 3E9 sterically clashes with TfR1 and Tf molecules. Superimposition of
195 4F7, 6H1 and 10B12 crystal structures onto the ternary complex structure shows that
196 this collection of antibodies does not inhibit by blocking the sites of interaction with
197 TfR1 or Tf, but rather through steric hindrance with the reticulocyte membrane (Fig.
198 4d). While all these antibodies target the N-terminal domain of PvRBP2b, future work
199 will need to determine if antibodies against the C-terminal domain will be effective at
200 blocking PvRBP2b interaction with TfR1.

201 The cryo-EM single particle analysis of the PvRBP2b-TfR1-Tf complex
202 identified crucial interfaces between PvRBP2b and TfR1 required for complex
203 formation. While *P. vivax* harbors more global genetic diversity relative to *P.*
204 *falciparum*, we show that PvRBP2b residues crucial for complex formation are
205 conserved across >200 field isolates from Asia Pacific^{20,24}. The crystal structures of
206 the inhibitory antibody fragments with PvRBP2b provide mechanistic insight on the
207 modes of action that involve steric hindrance with either the receptor or the
208 reticulocyte membrane. These high-resolution structures provide a solid structural
209 framework for the rational design of a promising vaccine candidate to block *P. vivax*
210 invasion into reticulocytes.

211

212

213 **References**

- 214 1. Mueller, I. *et al.* Key gaps in the knowledge of *Plasmodium vivax*, a neglected
215 human malaria parasite. *Lancet Infect. Dis.* **9**, 555–566 (2009).
- 216 2. Gruszczyk, J. *et al.* Transferrin receptor 1 is a reticulocyte-specific receptor for
217 *Plasmodium vivax*. *Science* **359**, 48–55 (2018).
- 218 3. Tham, W.-H. *et al.* Complement receptor 1 is the host erythrocyte receptor for
219 *Plasmodium falciparum* PfRh4 invasion ligand. *Proc. Natl. Acad. Sci. U. S. A.* **107**,
220 17327–17332 (2010).
- 221 4. Horuk, R. *et al.* A receptor for the malarial parasite *Plasmodium vivax*: the
222 erythrocyte chemokine receptor. *Science* **261**, 1182–1184 (1993).
- 223 5. Miller, L. H., Mason, S. J., Dvorak, J. A., McGinniss, M. H. & Rothman, I. K.
224 Erythrocyte receptors for (*Plasmodium knowlesi*) malaria: Duffy blood group
225 determinants. *Science* **189**, 561–563 (1975).
- 226 6. Adams, J. H. *et al.* The Duffy receptor family of *Plasmodium knowlesi* is located
227 within the micronemes of invasive malaria merozoites. *Cell* **63**, 141–153 (1990).
- 228 7. Cowman, A. F., Tonkin, C. J., Tham, W.-H. & Duraisingh, M. T. The Molecular
229 Basis of Erythrocyte Invasion by Malaria Parasites. *Cell Host Microbe* **22**, 232–
230 245 (2017).
- 231 8. Maier, A. G. *et al.* *Plasmodium falciparum* erythrocyte invasion through
232 glycophorin C and selection for Gerbich negativity in human populations. *Nat.*
233 *Med.* **9**, 87–92 (2003).
- 234 9. Crosnier, C. *et al.* Basigin is a receptor essential for erythrocyte invasion by
235 *Plasmodium falciparum*. *Nature* **480**, 534–537 (2011).

- 236 10. WHO | World Malaria Report 2016. WHO Available at:
237 <http://www.who.int/malaria/publications/world-malaria-report-2016/report/en/>.
238 (Accessed: 27th November 2017)
- 239 11. Hegner, R. Relative frequency of ring-stage plasmodia in reticulocytes and
240 mature erythrocytes in man and monkey. *Am. J. Epidemiol.* **27**, 690–718 (1938).
- 241 12. Carlton, J. M. *et al.* Comparative genomics of the neglected human malaria
242 parasite *Plasmodium vivax*. *Nature* **455**, 757–763 (2008).
- 243 13. Galinski, M. R., Medina, C. C., Ingravallo, P. & Barnwell, J. W. A
244 reticulocyte-binding protein complex of *Plasmodium vivax* merozoites. *Cell* **69**,
245 1213–26 (1992).
- 246 14. Gruszczyk, J. *et al.* Structurally conserved erythrocyte-binding domain in
247 *Plasmodium* provides a versatile scaffold for alternate receptor engagement. *Proc.*
248 *Natl. Acad. Sci. U. S. A.* **113**, E191-200 (2016).
- 249 15. Lawrence, C. M. *et al.* Crystal structure of the ectodomain of human
250 transferrin receptor. *Science* **286**, 779–782 (1999).
- 251 16. Lebron, J. A. *et al.* Crystal structure of the hemochromatosis protein HFE and
252 characterization of its interaction with transferrin receptor. *Cell* **93**, 111–123
253 (1998).
- 254 17. Abraham, J., Corbett, K. D., Farzan, M., Choe, H. & Harrison, S. C. Structural
255 basis for receptor recognition by New World hemorrhagic fever arenaviruses. *Nat.*
256 *Struct. Mol. Biol.* **17**, 438–444 (2010).
- 257 18. Radoshitzky, S. R. *et al.* Transferrin receptor 1 is a cellular receptor for New
258 World haemorrhagic fever arenaviruses. *Nature* **446**, 92–96 (2007).
- 259 19. Cheng, Y., Zak, O., Aisen, P., Harrison, S. C. & Walz, T. Structure of the
260 human transferrin receptor-transferrin complex. *Cell* **116**, 565–576 (2004).

- 261 20. Pearson, R. D. *et al.* Genomic analysis of local variation and recent evolution
262 in *Plasmodium vivax*. *Nat. Genet.* **48**, 959–964 (2016).
- 263 21. Demogines, A., Abraham, J., Choe, H., Farzan, M. & Sawyer, S. L. Dual host-
264 virus arms races shape an essential housekeeping protein. *PLoS Biol.* **11**, e1001571
265 (2013).
- 266 22. Radoshitzky, S. R. *et al.* Receptor determinants of zoonotic transmission of
267 New World hemorrhagic fever arenaviruses. *Proc. Natl. Acad. Sci. U. S. A.* **105**,
268 2664–2669 (2008).
- 269 23. Mikolajczak, S. A. *et al.* Plasmodium vivax Liver Stage Development and
270 Hypnozoite Persistence in Human Liver-Chimeric Mice. *Cell Host Microbe* **17**,
271 526–535 (2015).
- 272 24. Neafsey, D. E. *et al.* The malaria parasite *Plasmodium vivax* exhibits greater
273 genetic diversity than *Plasmodium falciparum*. *Nat. Genet.* **44**, 1046–1050 (2012).

274 **Acknowledgments** We thank Janet Newman from CSIRO Collaborative
275 Crystallization Centre for assistance with setting up the crystallization screens, the
276 Walter and Eliza Hall Institute’s Monoclonal Antibody Facility for production of
277 antibodies, and the MX and SAXS beamline staff at the Australian Synchrotron for
278 their assistance during data collection. This work was supported in part by the
279 Australian Research Council Future Fellowship to W.H.T. and M.D.W.G., a Speedy
280 Innovation Grant to W.H.T. and a National Health and Medical Research Council
281 fellowship (1105754) to J.M.M. W.H.T. is a Howard Hughes Medical Institute-
282 Wellcome Trust International Research Scholar (208693/Z/17/Z). R.D.P. is funded by
283 Wellcome Trust (090770). The authors acknowledge support from the Drakensberg
284 Trust, the Victorian State Government Operational Infrastructure Support and
285 Australian Government NHMRC IRIISS.

286 **Author Contributions**

287 J.G., L.J.C. and S.M. established experimental procedures. J.G. and W.W. optimized
288 the samples for cryo-EM. R.K.H., C.H. and Z.Y. performed specimen preparation for
289 cryo-EM, collected and processed the data, and generated the maps. J.G. carried out
290 model building, refinement and analysed the structure of PvRBP2b-TfR1-Tf complex.
291 J.G., L.J.C. and S.M. expressed and purified all mutants and performed the structure-
292 function analyses. L.J.C. and J.G. purified the Fab fragments. J.G. crystallized,
293 collected data and solved the structures of Fab complexes. J.M. and J.G. were
294 involved in the SAXS data collection. Y.F.M. and M.D.W.G. collected and analysed
295 AUC data. R.D.P. performed the sequence diversity analyses. W.H.T., J.G. and
296 A.F.C. designed the project. W.H.T., J.G. and Z.Y. analysed the data, and W.H.T. and
297 J.G. principally wrote the manuscript which was finalised with input from all authors.

298

299 **Author Information**

300 The authors declare no competing financial interests.

301

302

303

304

305

306

307

308

309

310

311 **Figure Legends**

312 **Figure 1.** The cryo-EM structure of PvRBP2b-TfR1-Tf ternary complex at 3.7 Å
313 resolution. a, Structure of PvRBP2b₁₆₈₋₆₃₃ in two orthogonal views with the secondary
314 structure labeled. b, The two-ligand PvRBP2b-TfR1-Tf ternary complex in two
315 orthogonal views. TfR1, Tf, PvRBP2b and ferric ions (Fe³⁺) are in green, cyan, violet
316 and as red spheres. c, The ternary complex relative to the reticulocyte membrane.
317 PvRBP2b is divided into N-terminal (violet) and C-terminal (blue) domains. The
318 apical, helical and protease-like domains of TfR1 are shown in green, yellow and red,
319 with the transmembrane (TM) and cytoplasmic domains of TfR1 indicated. Tf (cyan)
320 with Fe³⁺ as red spheres.

321 **Figure 2.** The PvRBP2b-TfR1-Tf interface. a, Surface representation of the
322 PvRBP2b-TfR1-Tf complex. The apical, helical and protease-like domains of TfR1
323 are in green, yellow and red. Tf, N- and C-terminal domains of PvRBP2b are in cyan,
324 violet and blue. TfR1 and Tf residues involved in the interaction with N- and C-
325 terminal domain of PvRBP2b are in violet and blue. For PvRBP2b, the footprints of
326 TfR1 and Tf are highlighted in green, red and cyan. b, Residues of PvRBP2b that bind
327 the receptor with hydrophobic interactions, hydrogen bonds and salt bridges are in
328 yellow, green and red. c, The interaction sites between PvRBP2b, TfR1 and Tf.
329 Residues forming important contacts are shown as sticks and labeled. Proteins are
330 colored according to the domain organization and as in a. d, Polymorphic residues
331 labeled as pink spheres are mapped on the structure of PvRBP2b shown in two
332 orthogonal views. Regions interacting with TfR1 and Tf are shown in green and cyan.
333 e, Schematic of the PvRBP2b sequence. Residues involved in binding and forming
334 hydrogen bonds and salt bridges are indicated with arrows above the sequence and

335 color-coded as in the left panel. Polymorphic residues are indicated with pink arrows
336 below the sequence.

337 **Figure 3.** Structure function analyses of PvRBP2b and TfR1 residues involved in
338 reticulocyte binding and complex formation. a, PvRBP2b mutant proteins analyzed
339 using reticulocyte-binding assay. Mean \pm S.E.M, n = 4, open circles represent
340 biological replicates. b, Analytical SEC for PvRBP2b mutants that bind to TfR1
341 residues. c, Analytical SEC for PvRBP2b mutants that bind to Tf residues. d,
342 Analytical SEC for TfR1 mutants. e, Schematic diagrams summarizing the mutational
343 analyses of PvRBP2b and TfR1. Mutants which showed no defect, moderate defect
344 and complete defect were colour coded as green, orange and red respectively. The key
345 interactions between PvRBP2b and TfR1 are highlighted as a dashed line for stacking
346 interactions or double lines for salt bridges. All analytical SEC in b and d were
347 performed once.

348 **Figure 4.** Structural modes of inhibition for anti-PvRBP2b antibodies. a, PvRBP2b
349 binding in the presence of anti-PvRBP2b mAbs 3E9, 4F7, 6H1, 8G7, 10B12 and anti-
350 PfRh4 mAb 10C9. Normalized binding results where PvRBP2b binding in the
351 absence of mAbs was arbitrarily assigned to be 100%. Mean \pm S.E.M, n = 4, open
352 dots represent biological replicates. b, Crystal structures of PvRBP2b (purple) bound
353 to inhibitory antibody fragments of 3E9, 4F7 and 6H1, and SAXS-based model for
354 10B12 antibody fragment complex. c, Surface representation of PvRBP2b molecule
355 with TfR1 (green), Tf (cyan) and the inhibitory antibodies interaction sites
356 highlighted. d, Superimposition of the structures of 3E9, 4F7, 6H1 and 10B12
357 antibodies fragments on the cryo-EM structure of the PvRBP2b-TfR1-Tf complex.

358

359

360 **Methods**

361 **Expression and purification of recombinant PvRBP2b and TfR1 mutants.** Protein
362 expression and purification for wildtype PvRBP2b, wildtype TfR1 and Tf were
363 performed as described previously². Mouse Tf was purchased from Sigma-Aldrich.
364 Restriction free cloning was used to generate the alanine mutants in both PvRBP2b
365 and TfR1 with all sequences verified using the Melbourne Translational Genomics
366 Center. Expression and purification of all mutant proteins were performed as for the
367 wildtype proteins. The complex between PvRBP2b, TfR1 and Tf was prepared by
368 mixing equimolar amounts of each protein to a final concentration of 1.0 mg/ml in
369 buffer containing 20 mM NaHEPES pH 7.5, 100 mM NaCl and 50 mM NaHCO₃. The
370 sample was flash-frozen in liquid nitrogen after the addition of 10% (v/v) glycerol,
371 and stored at -80°C. Circular dichroism experiments were performed as described
372 previously² to compare the secondary structure of wildtype vs mutant proteins.

373 **Cryo-EM sample preparation and data acquisition.** Prior to grid preparation, an
374 aliquot of protein was thawed on ice immediately followed by glycerol removal using
375 a 0.5 µl 100 kDa MWCO Amicon filtration unit (Millipore, Darmstadt Germany) at
376 4°C and 2,000 x g for 5 cycles. 3.2 µl of sample in glycerol-free buffer (20 mM
377 NaHEPES pH 7.5, 100 mM NaCl and 50 mM NaHCO₃) was applied to a glow-
378 discharged 400-mech quantifoil 1.2/1.3 Au grid (Quantifoil, Großlobichau Germany)
379 then rapidly plunge-frozen into a liquid ethane bath on a Vitrobot (FEI company, part
380 of Thermo Fisher Scientific Hillsboro, OR). Data were acquired at a sampling rate of
381 1.35 Å/pixel on a FEI Titan Krios at 300 kV equipped with spherical aberration
382 corrector and a post-energy filter K2 direct electron detector. Each exposure was
383 recorded with total dose of ~80 electron/Å² at a frame rate of 0.3 s per frame.

384 **Image processing and reconstruction.** Motion and drift in each image stack was
385 measured, corrected, and dose-weighted by unblur and sum_movie at 1.65 electron/Å²
386 per frame²⁵. 3,000 particles were manually picked in EMAN2²⁶ followed by 2D class
387 averages calculation in Relion. The preliminary 2D class averages were used to
388 generate a template for automated particle picking. CTF determination for each drift-
389 corrected micrograph was calculated by CTFIND4²⁷. We used Relion1.4 and
390 Relion2.0²⁸ for particle picking, extraction, 2D and 3D classifications, and high-
391 resolution refinement to derive final reconstructions for one-ligand and two-ligand
392 bound complexes. 3D classification was performed without imposing any
393 symmetry. As a result, one-ligand and two-ligand subclasses were identified. One-
394 ligand complex continued to be refined without symmetry applied. The two-ligand
395 class was refined independently in both C1 and C2 symmetry, and both refinements
396 yielded nearly identical high-resolution reconstructions (3.74 vs. 3.68Å). The
397 difference between C1 and C2-applied maps is negligibly minor indicating transient
398 heterogeneity was not detected under the current resolution limit. Therefore, C2
399 symmetry was applied in local refinements and post-processing to generate the final
400 reconstructed map of the two-ligand complex.

401 **Model building and refinement.** The program Chimera²⁹ was initially employed to
402 dock the available crystal structures into the electron density maps obtained from
403 cryo-EM. We used the following models: for TfR1 PDB accession code 1CX8¹⁵, for
404 Tf PDB accession code 3QYT³⁰ and for the N-terminal domain of PvRBP2b (residues
405 169-470) PDB accession code 5W53². For Tf, we observed some conformational
406 differences between the model and electron density and to facilitate the fitting we
407 divided the molecule into three parts consisting of subdomain N1, N2 and C-lobe.
408 Model building and refinement was continued manually in COOT³¹. The C-terminal

409 domain of PvRBP2b (residues 471-633) was built *de novo*. The high resolution of this
410 region allowed unambiguous assignment of the side chains in the region interacting
411 with TfR1. We did not observe the electron density corresponding to residues 161 till
412 167 and 634 till 969.

413 The model of the ternary complex was refined in Phenix³² using real space
414 refinement. For the two-ligand complex, non-crystallographic symmetry (NCS) was
415 imposed on the corresponding chains of identical molecules. For one-ligand complex,
416 no NCS restraints were used. No secondary structure restraints were initially applied to
417 the model. The final assignment of secondary structures was performed using the
418 DSSP program³³ integrated in Chimera²⁹. The quality of the final models was
419 validated using MolProbity³⁴ and EMRinger³⁵. Electron density maps were visualized
420 using Chimera²⁹.

421 **Determination of field polymorphisms.** We determined naturally occurring field
422 polymorphisms using data from the May 2016 release of the MalariaGEN *P.*
423 *vivax* Genome Variation project. We selected all variants that passed filters and had a
424 non-reference allele frequency among all samples of > 0.1. These variants can be
425 accessed using the URL:

426 [https://www.malariagen.net/apps/pvgv/index.html?dataset=pvix_stable&workspace](https://www.malariagen.net/apps/pvgv/index.html?dataset=pvix_stable&workspace=workspace_1&view=cc42817a-d8dd-11e7-a74a-22000a4d9adb&state=table_variants)
427 [=workspace_1&view=cc42817a-d8dd-11e7-a74a-](https://www.malariagen.net/apps/pvgv/index.html?dataset=pvix_stable&workspace=workspace_1&view=cc42817a-d8dd-11e7-a74a-22000a4d9adb&state=table_variants)
428 [22000a4d9adb&state=table_variants](https://www.malariagen.net/apps/pvgv/index.html?dataset=pvix_stable&workspace=workspace_1&view=cc42817a-d8dd-11e7-a74a-22000a4d9adb&state=table_variants).

429 **Antibodies production.** Anti-PvRBP2b mouse monoclonal antibodies were prepared
430 at the Walter and Eliza Hall Institute Monoclonal Antibody Facility as described
431 previously². 24 hybridomas were selected based on displaying the strongest antibody
432 response to PvRBP2b₁₆₁₋₁₄₅₄ as measured by ELISA. These hybridoma supernatants
433 were screened for the ability to inhibit PvRBP2b₁₆₁₋₁₄₅₄ binding to reticulocytes.

434 Selected hybridomas producing inhibitory antibodies were cloned by limiting dilution
435 in multi-well plates aiming for one cell or less per well. The sub-cloned cell
436 supernatants were screened by ELISA against PvRBP2b₁₆₁₋₁₄₅₄. Two or more rounds
437 of limiting dilution cloning were generally required before the hybridomas were
438 deemed monoclonal. The antibodies were purified from monoclonal hybridoma
439 supernatants with Protein A Sepharose. All monoclonal antibodies used for protein
440 crystallization have been sequenced by GenScript Company.

441 **Flow cytometry-based reticulocyte-binding assay.** Enriched reticulocytes were
442 resuspended in phosphate buffered saline (PBS) to a final volume of 1×10^7 cells/ml.
443 Recombinant proteins were incubated at 0.02 mg/ml in 50 μ l of the resuspended
444 reticulocytes for one hour at room temperature. All washes were performed in PBS
445 supplemented with 1% (w/v) bovine serum albumin (BSA) and spun at $4,000 \times g$ for 1
446 minute. All antibody incubations were performed at room temperature for one hour.
447 Binding assays were washed once and incubated with the respective rabbit polyclonal
448 antibodies (12.5 μ g/ml). After washing, Alexa Fluor 647 chicken anti-rabbit
449 secondary antibody (1:100; Life Technologies) was added. After a final wash, 100 μ l
450 thiazole orange (TO) (Retic-Count Reagent; BD Biosciences) was added and
451 incubated for half an hour. Reticulocytes with bound proteins were resuspended in
452 200 μ l PBS and analysed on the LSR II flow cytometer (BD Biosciences). 50,000
453 events were recorded and results were analysed using FlowJo software (Three Star).
454 The background signal from a rabbit polyclonal antibody and Alexa Fluor 647
455 conjugated antibody control (without protein) was subtracted from all binding results.
456 To enable comparison between biological repeats, the percentage binding of the
457 protein in the presence of mAbs was divided by the percentage binding with no mAbs

458 and multiplied by 100 to obtain the percentage binding relative to the no inhibitor
459 control.

460 **Analytical size exclusion chromatography.** Liquid chromatography was performed
461 using ÄKTA pure 25 M1 chromatographic system (GE Healthcare). Proteins were
462 mixed in equimolar ratio one hour prior to the analysis and the same amount of
463 protein was used throughout the experiment. 100 μ l was injected onto Superdex 200
464 Increase 10/300 GL column (GE Healthcare) equilibrated with the buffer containing
465 20 mM NaHEPES pH 7.5, 100 mM NaCl, 50 mM NaHCO₃ at 0.75 ml/min of buffer
466 flow. The absorbance of the eluent was monitored at 280 nm. Eluates were collected
467 in 0.5 ml fractions and analyzed using SDS-PAGE. All steps were performed at room
468 temperature.

469 **Analytical ultracentrifugation.** Sedimentation velocity experiments were performed
470 using an XL-I analytical ultracentrifuge (Beckman Coulter) equipped with UV/Vis
471 scanning optics. Samples were prepared containing a constant concentration of 2.5
472 μ M TfR1-Tf complex and PvRBP2b₁₆₁₋₉₆₉ at concentrations of 0.25, 0.5, 1.0, 2.0, 4.0,
473 8.0, and 16.0 μ M. Buffer reference (20 mM NaHEPES pH 7.5, 100 mM NaCl, 50
474 mM NaHCO₃) and sample solutions were loaded into 12 mm double-sector cells with
475 quartz windows and the cells were mounted in an An-50Ti 8-hole rotor.
476 Centrifugation was conducted at 35,000 rpm (98,780 \times g) at 20°C, and radial
477 absorbance data were collected at 250 nm in continuous mode. Data were fitted to a
478 continuous sedimentation coefficient distribution [$c(s)$] model and distributions were
479 integrated between 9 S and 13 S using SEDFIT³⁶ to determine the integrated
480 absorbance signal. Buffer density and viscosity were calculated using SEDNTERP³⁷.

481 **Fab fragment purification and formation of Fab-PvRBP2b complexes.** Mouse
482 monoclonal antibodies were digested using papain (Sigma-Aldrich) for two hours at

483 room temperature. For 6H1 and 10B12, L-cysteine (Sigma-Aldrich) was added to
484 cleave F(ab')₂ fragments. An excess of iodoacetamide (Sigma-Aldrich) was added to
485 halt the reaction and the samples were passed through a protein A column (GE
486 Healthcare). The flow-through was concentrated and applied on a S75 Superdex
487 16/600 column (GE Healthcare) equilibrated with a buffer containing 20 mM
488 NaHEPES pH 7.5 and 150 mM NaCl. Protein samples were flash-frozen in liquid
489 nitrogen after addition of 10% (v/v) glycerol, and stored at -80°C until further
490 processing.

491 Recombinant PvRBP2b fragment PvRBP2b₁₆₉₋₄₇₀ was mixed with molar
492 excess of individual Fab fragments and incubated overnight at 4°C to allow complex
493 formation and purified using SEC. Fractions containing the complexes were
494 concentrated down using Vivaspin 15 Turbo centrifugal concentrators (Sartorius) with
495 a 5 kDa molecular weight cut-off in a buffer containing 20 mM NaHEPES pH 7.5 and
496 150 mM NaCl and used for crystallization.

497 **Protein crystallization.** Crystallization trials were performed at the CSIRO
498 Collaborative Crystallization Center using two different protein concentrations, 7.5
499 and 15 mg/ml. Crystals of 3E9 in complex with the N-terminal domain of PvRBP2b
500 were obtained in 0.2 M KBr, 15% (w/v) PEG 4,000 and 0.05 M sodium citrate/citric
501 acid pH 5.5. Crystals of 4F7 Fab fragment alone were obtained in 20% (w/v) PEG
502 4,000, 0.05 M sodium citrate/citric acid pH 5.5 and 20% (v/v) 2-propanol. Crystals of
503 4F7 in complex with the N-terminal domain of PvRBP2b were obtained in 0.2 M
504 trisodium citrate and 20% (w/v) PEG 3,350. Crystals of 10B12 Fab fragment alone
505 were obtained in 20% (w/v) PEG 4,000, 0.1 M sodium citrate/citric acid pH 5.5 and
506 20% (v/v) 2-propanol. Crystals of 6H1 in complex with the N-terminal domain of
507 PvRBP2b were obtained in 0.2 M (NH₄)₂SO₄ and 20% (w/v) PEG 3,350.

508 **Data collection and structure solution.** Crystals were cryo-protected in a reservoir
509 solution supplemented with 20% (v/v) glycerol and flash-frozen in liquid nitrogen.
510 Diffraction data were collected at MX2 beamline at the Australian Synchrotron
511 Facility in Clayton, Australia at 0.9537 Å wavelength using ADSC Quantum 315r
512 detector. Data were integrated using iMosflm³⁸. Scaling and merging were performed
513 using program Aimless from the CCP4 package³⁹. Cell content was analyzed using
514 the program Matthews⁴⁰. Molecular replacement for the data collected for 4F7 Fab
515 fragment alone was performed using Phaser⁴¹ with an unrelated antibody as a model
516 (PDB accession code 5EN2). The model obtained together with the structure of the N-
517 terminal domain of PvRBP2b (PDB accession code 5W53) were used to solve
518 structures of 3E9, 4F7 and 6H1 Fab complexes. The crystals for 10B12 contained
519 only the Fab fragment. Initial models were rebuilt automatically using the program
520 AutoBuild³² followed by a manual improvement using the program Coot¹⁴. The
521 structures were refined using the program Phenix Refine³² and included TLS
522 (translation/libration/screw) motions that were generated using the TLSMD web
523 server⁴². Crystallographic data collection and refinement statistics for all structures
524 are summarized in Extended Data Table 3. Figures were prepared using either Pymol
525 (<http://www.pymol.org>) or Chimera²⁹.

526 **Small angle X-ray scattering.** SAXS experiments were performed as described
527 previously^{2,14}. We docked the crystal structures of the N-terminal domain of
528 PvRBP2b and 10B12 Fab fragment into the SAXS envelope of the 10B12-PvRBP2b
529 complex using program Collage from the Situs Program Package⁴³. Due to the
530 symmetry of the SAXS envelope and the Fab fragment, we could not unambiguously
531 assign the identity of the heavy and light chains within the model.

532

533 **Data availability**

534 The cryo-EM maps have been deposited in the Electron Microscopy Data Bank with
535 accession codes EMD-7783, EMD-7784 and EMD-7785. The coordinates of the
536 atomic models have been deposited in the Protein Data Bank under accession codes
537 PDB 6D03, PDB 6D04 and PDB 6D05 for the PvRBP2b-Tf-TfR1 one-ligand
538 complex, two-ligand complex subclass 1 and subclass 2, respectively. Coordinates
539 and structure factors have been deposited in the Protein Data Bank under accession
540 codes 6BPA (PvRBP2b-3E9 complex), 6BPB (4F7 Fab alone), 6BPC (PvRBP2b-4F7
541 complex), 6BPD (10B12 Fab alone) and 6BPE (PvRBP2b-6H1 complex).

542 **References**

- 543 25. Grant, T. & Grigorieff, N. Measuring the optimal exposure for single particle
544 cryo-EM using a 2.6 Å reconstruction of rotavirus VP6. *eLife* **4**, e06980 (2015).
- 545 26. Tang, G. *et al.* EMAN2: an extensible image processing suite for electron
546 microscopy. *J. Struct. Biol.* **157**, 38–46 (2007).
- 547 27. Rohou, A. & Grigorieff, N. CTFFIND4: Fast and accurate defocus estimation
548 from electron micrographs. *J. Struct. Biol.* **192**, 216–221 (2015).
- 549 28. Scheres, S. H. W. RELION: Implementation of a Bayesian approach to cryo-
550 EM structure determination. *J. Struct. Biol.* **180**, 519–530 (2012).
- 551 29. Goddard, T. D., Huang, C. C. & Ferrin, T. E. Visualizing density maps with
552 UCSF Chimera. *J. Struct. Biol.* **157**, 281–287 (2007).
- 553 30. Yang, N., Zhang, H., Wang, M., Hao, Q. & Sun, H. Iron and bismuth bound
554 human serum transferrin reveals a partially-opened conformation in the N-lobe.
555 *Sci. Rep.* **2**, 999 (2012).
- 556 31. Emsley, P., Lohkamp, B., Scott, W. G. & Cowtan, K. Features and
557 development of Coot. *Acta Crystallogr Biol Crystallogr* **66**, 486–501 (2010).

- 558 32. Adams, P. D. *et al.* PHENIX: a comprehensive Python-based system for
559 macromolecular structure solution. *Acta Crystallogr Biol Crystallogr* **66**, 213–21
560 (2010).
- 561 33. Kabsch, W. & Sander, C. Dictionary of protein secondary structure: pattern
562 recognition of hydrogen-bonded and geometrical features. *Biopolymers* **22**, 2577–
563 2637 (1983).
- 564 34. Chen, V. B. *et al.* MolProbity: all-atom structure validation for
565 macromolecular crystallography. *Acta Crystallogr. D Biol. Crystallogr.* **66**, 12–21
566 (2010).
- 567 35. Barad, B. A. *et al.* EMRinger: side chain-directed model and map validation
568 for 3D cryo-electron microscopy. *Nat. Methods* **12**, 943–946 (2015).
- 569 36. Schuck, P. Size-distribution analysis of macromolecules by sedimentation
570 velocity ultracentrifugation and Lamm equation modeling. *Biophys. J.* **78**, 1606–
571 1619 (2000).
- 572 37. *Analytical ultracentrifugation in biochemistry and polymer science* /. (Royal
573 Society of Chemistry, c1992.).
- 574 38. Battye, T. G., Kontogiannis, L., Johnson, O., Powell, H. R. & Leslie, A. G.
575 iMOSFLM: a new graphical interface for diffraction-image processing with
576 MOSFLM. *Acta Crystallogr Biol Crystallogr* **67**, 271–81 (2011).
- 577 39. Winn, M. D. *et al.* Overview of the CCP4 suite and current developments.
578 *Acta Crystallogr Biol Crystallogr* **67**, 235–42 (2011).
- 579 40. Kantardjieff, K. A. & Rupp, B. Matthews coefficient probabilities: Improved
580 estimates for unit cell contents of proteins, DNA, and protein-nucleic acid complex
581 crystals. *Protein Sci* **12**, 1865–71 (2003).

- 582 41. McCoy, A. J. *et al.* Phaser crystallographic software. *J Appl Crystallogr* **40**,
583 658–674 (2007).
- 584 42. Painter, J. & Merritt, E. A. TLSMD web server for the generation of multi-
585 group TLS models. *J Appl Crystallogr* **39**, 109–111 (2006).
- 586 43. Birmanns, S., Rusu, M. & Wriggers, W. Using Sculptor and Situs for
587 simultaneous assembly of atomic components into low-resolution shapes. *J. Struct.*
588 *Biol.* **173**, 428–435 (2011).

589 **Figure Legends for Extended Data**

590 **Extended Data Figure 1.** Details of the cryo-EM data collection and analysis. a,
591 Coomassie-stained reducing SDS-PAGE gel of the proteins used for the sample
592 preparation. M - molecular weight marker (molecular weight of protein standards is
593 given in kDa). For gel source data, see Supplementary Figure 1. b, Representative
594 micrograph of the sample after drift correction and dose-weighting. c, Representative
595 2D class averages. 2D class averages exhibit different projections corresponding to
596 each orientation. d, 3D classification effectively separated two groups of populations.
597 On the left: TfR1-Tf complex with bound one PvRBP2b molecule. On the right:
598 TfR1-Tf complex with bound two PvRBP2b molecules. TfR1-Tf is shown in blue and
599 PvRBP2b in pink. Scale bar is displayed as labeled. e, Local resolution estimation
600 diagram of the final refined maps. On the left: One-ligand complex. On the right:
601 Two-ligand complex. Resolution keys are labeled from 3.5 to 6.0 Å. f, Resolution
602 estimation of the cryo-EM map. Fourier-shell-correlation (FSC) plot showing the
603 resolutions at 0.143 FSC (drawn in a dashed line) for both complexes determined by
604 gold-standard method. g, Representative EM density for different parts of C-terminal
605 domain of PvRBP2b. Some of the residues are also indicated. h, FSC curves of the
606 final refined model versus the final cryo-EM map (full dataset, blue), of the outcome

607 of model refinement with a half map versus the same map (red), and of the outcome
608 of model refinement with a half map versus the other half map (green). For panels a to
609 c, the experiment was performed once.

610 **Extended Data Figure 2.** Detailed structural analyses of PvRBP2b and sedimentation
611 velocity analysis of the formation of the ternary PvRBP2b₁₆₁₋₉₆₉-TfR1-Tf complex. a,
612 Superimposition of the cryo-EM based structure of PvRBP2b with the previously
613 reported crystal structure of the N-terminal domain (PDB accession number 5W53).
614 b, Two orthogonal views of PvRBP2b shown in surface representation and colored
615 according to the potential on the surface of the molecule. Electrostatic surface
616 potential was calculated using program APBS integrated in Chimera with the
617 nonlinear Poisson-Boltzmann equation and contoured at ± 5 kT/e. Negatively and
618 positively charged surface areas are colored in red and blue, respectively. c,
619 Continuous sedimentation coefficient [c(s)] distributions for the TfR1-Tf complex
620 (2.5 μ M complex) in the presence of increasing concentrations of PvRBP2b₁₆₁₋₉₆₉
621 (0.25-16 μ M). The configuration and surface charge properties of the ternary complex
622 suggest that this particle may display non-ideal sedimentation, possibly contributing
623 to the shift in sedimentation coefficient observed. Thus, the integrated absorbance
624 signal in the fast sedimenting peak of the distributions was analysed as a function of
625 PvRBP2b₁₆₁₋₉₆₉ concentration. d, Here the TfR1-Tf complex was assumed to sediment
626 as a single, stable species. These data are consistent with the binding of two
627 molecules of PvRBP2b₁₆₁₋₉₆₉ to the TfR1-Tf complex with macroscopic dissociation
628 constants in the mid-nanomolar to low-micromolar range. e, Residuals for the best fit
629 of the raw radial absorbance sedimentation velocity data to a c(s) distribution model
630 for 2.5 μ M of TfR1-Tf in the presence of (respectively from top to bottom): 0.25 μ M,
631 0.5 μ M, 1.0 μ M, 2.0 μ M, 4.0 μ M, 8.0 μ M and 16.0 μ M of PvRBP2b₁₆₁₋₉₆₉.

632 **Extended Data Figure 3.** Structure of the one-ligand complex and conformational
633 changes induced in TfR1 upon PvRBP2b binding. a, Overall view of the one-ligand
634 complex. Proteins are shown in ribbon representation. Molecule of TfR1 interacting
635 with PvRBP2b is colored according to domain organization with protease-like domain
636 in red, apical domain in green and helical domain in yellow. The other molecule of
637 TfR1 that remains unliganded is colored in wheat. Tf is colored in cyan with ferric
638 ions Fe³⁺ shown as red spheres. The N- and C-terminal domains of PvRBP2b are
639 shown in violet and blue, respectively. b, Superimposition of the unliganded TfR1
640 molecule from one-ligand complex on the ligand-bound TfR1 from two-ligand
641 complex. The color-code as in a. The movement of the apical domain has been
642 schematically indicated by a black arrow. For clarity, both Tf molecules have been
643 omitted. c, Closer view of the superimposition shown in panel b. The residues that are
644 affected the most by PvRBP2b binding are shown as sticks and labeled. d, The
645 superimposition of TfR1 in complex with Tf and PvRBP2b (colored according to the
646 domain) and TfR1 in the complex with Tf only (in grey, PDB accession number
647 3S9L). The r.m.s.d. between 1,090 aligned atoms C α is 0.81 Å. The movement of the
648 apical domain is schematically represented with black arrows. e, Superimposition of
649 Tf in cryo-EM structure of PvRBP2b-TfR1-Tf complex (in cyan) with the crystal
650 structure of holo-Tf in Tf-TfR1 complex (on the left, in wheat, PDB accession
651 number 3S9L) or with the crystal structure of holo-Tf (in the middle, in green, PDB
652 accession number 3V83) or with the structure of apo-Tf (on the right, in orange, PDB
653 accession number 2HAV). Iron ions are shown as red spheres. R.m.s.d. values are
654 indicated above each superimposition. f, Two orthogonal views of the
655 superimposition between two subclasses for two-ligand complex. Molecules are
656 shown in cartoon representation and colored in violet and cyan for subclass 1 and 2,

657 respectively. The most important difference between the two subclasses is the
658 movement of the N-terminal domain of PvRBP2b, which has been indicated with
659 black arrows. g, Close view of the PvRBP2b-Tf interaction site. The N2 subdomain of
660 Tf in the cryo-EM structure (in cyan) has been superimposed with the crystal
661 structures for holo-Tf in closed conformation (in wheat), holo-Tf in partially open
662 conformation (in green) and apo-Tf in open conformation (in orange). The movement
663 of the N1 subdomain has been schematically highlighted with the black arrows.

664 **Extended Data Figure 4.** Site-directed mutagenesis of PvRBP2b and TfR1. a, SDS-
665 PAGE gels of purified PvRBP2b mutant recombinant proteins. Two micrograms of
666 each protein were loaded onto a 4-12% NuPAGE gradient gel under reducing
667 conditions and stained with Coomassie Brilliant Blue. Molecular mass marker (M)
668 indicated in kDa. b, Circular dichroism spectra of recombinant PvRBP2b mutants. c,
669 Analytical SEC (left to right panel) of complex formation between PvRBP2b mutants
670 at residues Y538, Y542, K600 and Y604 with TfR1-Tf. The same representative
671 SDS-PAGE gels are used for wildtype PvRBP2b protein and for TfR1 Δ G217 mutant
672 protein SEC analyses. d, SDS-PAGE gel of purified TfR1 mutant recombinant
673 proteins. Two micrograms of each protein were loaded onto a 4-12% NuPAGE
674 gradient gel under reducing conditions and stained with Coomassie Brilliant Blue.
675 Molecular mass marker (M) indicated in kDa. e, Analytical SEC of TfR1 mutants in
676 complex with Tf. f, Circular dichroism spectra of recombinant TfR1 mutants. For all
677 panels, the experiments were performed once. For gel source data, see Supplementary
678 Figure 1.

679 **Extended Data Figure 5.** PvRBP2b interacts mostly with the residues specific for
680 human TfR1. a, Schematic representation of TfR1 sequence colored according to the
681 domain (apical in green, protease-like in red and helical in yellow). The limits of the

682 particular domains are indicated above the schematic. The most important residues
683 forming either hydrogen bonds or salt bridges with PvRBP2b are indicated below
684 with the black arrows and labeled. b, Comparison between Machupo virus GP1 and
685 PvRBP2b binding sites. Human TfR1 is shown in the center in surface representation
686 and colored according to the domain organization. The residues interacting with
687 PvRBP2b are colored in violet and those with Machupo virus GP1 in dark blue. The
688 residues overlapping between the two sites are colored in magenta. The surrounding
689 panels show fragments of the alignment between TfR1 sequences from different
690 species (human, mouse, rat, hamster, cat and dog). The amino acid residues are
691 colored according to their chemical properties (acidic residues shown in red, basic in
692 blue, polar in magenta, cysteines in yellow and hydrophobic in a scale of grey with
693 the intensity proportional to the residue hydrophobicity). The fragments of the
694 alignment corresponding to the apical and protease-like domains of TfR1 are
695 additionally shaded in green and red, respectively. The residues interacting with
696 PvRBP2b are indicated with stars above the alignment and colored according to the
697 type of the interaction (hydrogen bonds in green, salt bridges in red, other as empty
698 stars). The Machupo virus GP1 interaction site is indicated with a dark blue line. The
699 position of G217 deletion as well as the G142S polymorphism have been indicated
700 with black arrows above the alignment. c, Analytical SEC results showing
701 PvRBP2b₁₆₁₋₁₄₅₄ interaction with mouse Tf and TfR1. For gel source data, see
702 Supplementary Figure 1. The elution profiles for the separate components as well as
703 for the mix between them are shown on the top. Bottom panels presents the SDS-
704 PAGE gels for the particular fractions. Left panel: human Tf and human TfR1, middle
705 left panel: mouse Tf and human TfR1, middle right panel: human Tf and mouse TfR1,

706 right panel: mouse Tf and mouse TfR1. The same representative SDS-PAGE gel is
707 used for PvRBP2b protein SEC analyses. All analytical SEC were performed once.

708 **Extended Data Figure 6.** Reticulocyte-binding and SAXS data analyses for the N-
709 terminal domain of PvRBP2b in complexes with four different inhibitory Fab
710 fragments. a, PvRBP2b₁₆₁₋₁₄₅₄ binding in either the absence of mAbs or the presence
711 of anti-PvRBP2b mAbs (3E9, 4F7, 6H1, 8G7 and 10B12) or anti-PfRh4 mAb (10C9),
712 analysed by flow cytometry. Dot plots of PvRBP2b₁₆₁₋₁₄₅₄ binding (y-axis) to
713 reticulocytes stained with thiazole orange (TO, x-axis). This experiment was repeated
714 independently four times with similar results. b, Arbitrarily offset scattering intensity
715 profiles for the PvRBP2b-Fab complexes. The background-subtracted SAXS data are
716 shown as black open circles representing natural logarithm of mean intensity $\ln I(q)$ as
717 a function of momentum transfer q in \AA^{-1} (a.u. - arbitrary unit). The theoretical
718 scattering profiles (solid lines, PvRBP2b-3E9 in blue, PvRBP2b-4F7 in red,
719 PvRBP2b-6H1 in green and PvRBP2b-10B12 in yellow) calculated from the crystal
720 structures were fitted to the experimental scattering data using CRY SOL. c, Guinier
721 plots for $qR_g \leq 1.3$ showing that neither high-molecular-mass aggregates nor inter-
722 particle interference contributes measurably to scattering and the data are of high
723 quality (colors as in b). d, Pair-wise inter-atomic distance distribution function, $P(r)$
724 (colors as in b). e, Two orthogonal views of *ab initio* bead models represented as grey
725 spheres, superimposed with the crystal structure of the corresponding antibody
726 complexes. For PvRBP2b-10B12 complex, program COLLAGE was used to rigid
727 body fit two crystal structures, the N-terminal domain of PvRBP2b (PDB 5W53) and
728 the structure of the 10B12 Fab fragment alone. f, Table summarizing SAXS data
729 collection and analysis. The radius of gyration (R_g) and initial scattering intensity $I(0)$
730 were approximated using the Guinier equation with program PRIMUS. The R_g and

731 maximum particle dimension Dmax were calculated from the P(r) analysis using
732 program GNOM. The normalized spatial discrepancy parameter (NSD) indicates the
733 similarity between 20 independently generated *ab initio* models. The c parameter
734 provides the assessment of the fit of the average model to the experimental data
735 calculated using program CRY SOL. The structural parameters and their associated
736 errors are those derived by least-squares curve-fitting analysis of the scattering data as
737 formulated within the listed software packages.

738 **Extended Data Table 1.** Cryo-EM data collection, refinement and validation
739 statistics.

740 **Extended Data Table 2.** Summary of interactions between PvRBP2b and TfR1-Tf.
741 The distance measurements are based on molecules B, C and F in two-ligand complex
742 subclass 1.

743 **Extended Data Table 3.** Data collection and refinement statistics for PvRBP2b
744 complexes with Fab fragments. X-ray diffraction data were collected on single
745 crystals. * Values in parentheses are for highest-resolution shell.

746 **Extended Data Table 4.** Summary of interactions between PvRBP2b and
747 monoclonal antibodies 3E9, 4F7 and 6H1 Fab fragments. The distance measurements
748 are based on molecules A, B and C.

749

750

751

752

753

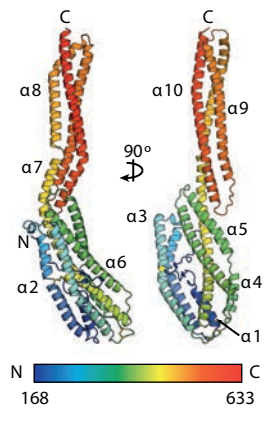
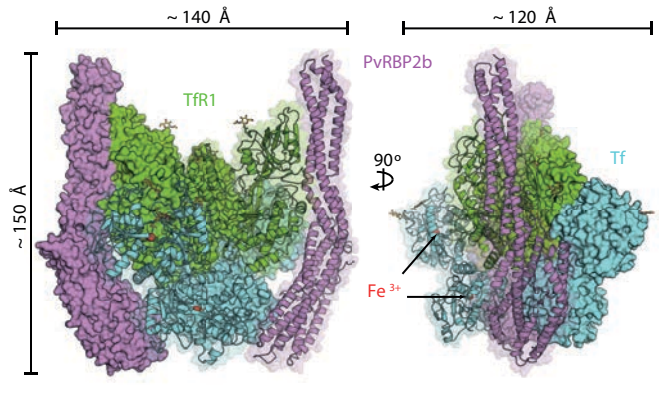
754

755

756

757

758

a**b****c**